PCCP

ROYAL SOCIETY OF CHEMISTRY

PAPER

Check for updates

Cite this: *Phys. Chem. Chem. Phys.*, 2021, **23**, 24294

Prediction of an Al_4C_4 superatom organic framework (SOF) material based on the superatom network model†

Jiuqi Yi,[a] Bingbing Gong,[b] Chang Xu, *[a] Wenhua Zhang *[b] and Longjiu Cheng *[ac]

Metal organic framework (MOF) materials have attracted significant attention due to their wide potential applications, but it is still a challenge to design MOFs with advanced properties by exploring novel metal nodes. In this study, a kind of superatom organic framework (SOF) material is proposed based on the superatom network (SAN) model. Tetrahedron Al_4 superatom unit is used as nodes in the MOF structure, and linear –C≡C– ligands are chosen as linkers. Localized chemical bonding analysis and nucleus-independent chemical shift (NICS) scan confirm that the Al_4 core keeps the superatom electronic shell in the SOF structure. Further calculations demonstrate that this Al_4C_4 crystal has high dynamic and thermal stabilities, with an indirect semiconductor band gap of 2.57 eV. Analysis of its optical properties indicates its potential applications as an optoelectronic device. This novel kind of SOF material has both porous framework as traditional MOFs and superatomic character in its nodes, indicating its unique potential properties. Our work would provide a new way for designing functional MOF materials.

Received 21st June 2021,
Accepted 6th October 2021

DOI: 10.1039/d1cp02798k

rsc.li/pccp

Introduction

During the past few decades, metal–organic frameworks (MOFs) have become one of the hottest topics in materials chemistry.[1–12] Due their unique chemical structures combining of organic and inorganic characters with high porosity and various interface phenomena, MOFs exhibit wild potential applications in gas storage, separations, catalysis, biomedicine and chemical sensing.[13–17] The first MOF was obtained by Yaghi *et al.* in 1995, which is a two dimensional coordination compound formed by pyridine ligands and cobalt atoms.[12] Following this study, a series of similar MOF materials was designed and investigated.[18] Traditional MOFs are composed of metal ions or clusters as nodes and organic ligands as linkers. The diversity of MOFs could be enriched by various metal nodes ranging from single atoms to diverse clusters, and increasing organic linkers with different lengths, geometric shapes and functional groups.[19,20] Moreover, the size and function of the pore space could be precisely adjusted at the molecular level using various building blocks and synthetic procedures.[21] However, it is still a challenge in exploring novel metal nodes for the design of MOFs with advanced properties.

Metal clusters with certain number of valence electrons have a similar electronic character and reaction properties as simple atoms, which are regarded as superatom (SA).[22–31] The electronic structures of spherical SA could be described by the Jellium model, in which valence electrons are delocalized over the whole clusters and filled SA valence orbital of $|1S^2|1P^6|1D^{10}|2S^2|1F^{14}|2P^6|\ldots$ and there are still other electron-counting rules for SA.[32–34] SAs with diverse electronic shell could mimic the chemistry of atoms in the periodic table, thus a new three-dimensional periodic table would be obtained with SAs constituting the third dimension.[35] In 1992, Jena *et al.* first proposed the idea that SAs can be used as building blocks for material assembling, and SA-assembled materials would exhibit unique properties as individual identities of SA are retained.[36] Since then, numbers of SA-assembled materials are reported experimentally and theoretically, and rules of SA-assembling are also explored by researchers.[28,37] In 2013, the superatom network (SAN) model was proposed by Cheng *et al.* to explore the electronic nature of large-scale ligand-protected metal clusters.[27] It has successfully explained electronic shell of a series of ligand-protected golden clusters, such as $[Au_{18}(SR)_{14}]$, $[Au_{20}(SR)_{16}]$, and $[Au_{24}(SR)_{20}]$. In this model, SAs are connected with each other through ligands with covalence bonds to form a network, and the SA core still retains the SA electronic shell.

---

[a] Department of Chemistry, Anhui University, Hefei, 230601, P. R. China. E-mail: xuchang1986@ahu.edu.cn, clj@ustc.edu
[b] Key Laboratory of Materials for Energy Conversion, CAS, University of Science and Technology of China, Hefei, Anhui 230026, P. R. China. E-mail: whhzhang@ustc.edu.cn
[c] Key Laboratory of Structure and Functional Regulation of Hybrid Materials (Anhui University), Ministry of Education, Hefei, 230601, P. R. China

† Electronic supplementary information (ESI) available. See DOI: 10.1039/d1cp02798k

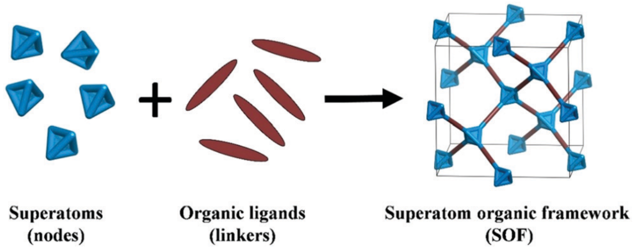

Fig. 1 Schematic of the general formation of SOFs through the assembly of superatom (nodes) and organic ligand (linkers) building units into a 3D structure.

This model reveals the electronic rules of certain ligand-protected metal clusters and gives references for the design of cluster-assembling materials.[38]

As SAs have multi-coordination capabilities as transition metals, they might be used instead of metal nodes in MOFs. In this study, a new type of MOF material with SA nodes are designed based on the SAN model (shown in Fig. 1) *via* density functional theory (DFT) calculations, which is defined as the SA organic framework (SOF). The tetrahedral Al_4 units, which have been successfully used in a series of cluster-assembling materials,[39–41] are chosen as building blocks of SA nodes, and the linear $-C{\equiv}C-$ ligands are used as organic linkers. Interestingly, this SOF material has high porosity as traditional MOFs, and the SA node keeps the superatomic electronic shell inside its structure depending on our investigation. Elastic constants, *ab initio* molecular dynamics (AIMD) and optical properties are also discussed to explore its potential applications.

Computational methods and details

In this article, calculations of the $Al_4(C{\equiv}CH)_4$ cluster were carried out using the Gaussian 09 package[42] at PBE/def2tzvp[43,44] levels of theory. Calculations of solid-state Al_4C_4 were carried out using the Vienna *Ab initio* Simulations Package (VASP)[45–48] with projector augmented wave (PAW) pseudopotentials[49,50] and the PBE density functional.[51] In addition, the HSE06 hybrid functional[52] has been used to reach more accurate electronic band structures. The plane-wave cutoff energy of 500 eV of the associated pseudopotentials was used. The Brillouin zone was sampled by the Monkhorst–Pack method[53] with an automatic generated grid of 6 × 6 × 6. During the optimization process, spin polarization was turned on, the Hellmann–Feynman force convergence criterion was less than 0.001 eV Å^{-1}, and the self-consistent field procedures were performed with an energy of 10^{-6} eV for the total energy. The calculations of the phonon spectra were done using the PHONOPY program.[54]

The climbing-image nudged elastic band (CI-NEB) method[55] was employed to investigate the kinetics of the O_2 adsorption process and relative activation energy of chemisorption. A unit cell containing 32 Al atoms and 32 C atoms was selected in our calculation, and seven intermediate images were used to predict the reaction path. The image of each CI-NEB simulation relaxed until the perpendicular forces were less than 0.02 $\text{eV}\cdot\text{Å}^{-1}$. Moreover, the DFT-D3 method[56] was used to consider the long-range van der Waals (vdW) force in the interaction of O_2 with the Al_4C_4 crystal. AIMD simulations were performed to examine the thermal stability of the Al_4C_4 assembled-structure, where the NVT (constant number, volume, and temperature) canonical ensemble was used. The AIMD simulation lasts for 5 ps with a time step of 1.0 fs at 700 K, and the temperatures were controlled using the Nosé–Hoover method.[57] In both CI-NEB and AIMD calculations, spin polarization was turned on.

Chemical bonding analyses were performed using the adaptive natural density partition (AdNDP)[58] for clusters and Solid State AdNDP (SSAdNDP)[59] method for solid materials, which were developed by Boldyrev *et al.* for discussing multicenter delocalized bonds.[38,60–65] Within SSAdNDP, the plane-wave density was projected[66] into the def2tzvp basis set. All the crystal structure was visualized using the VESTA software package.[67]

Results and discussion

Geometric and electronic characters of the $Al_4(C{\equiv}CH)_4$ cluster

First, the $Al_4(C{\equiv}CH)_4$ cluster is built and optimized as the basic units for our SOF material. The optimized structure is shown in Fig. 2a, which is composed of a tetrahedral Al_4 unit and four $-C{\equiv}CH$ ligands. This cluster maintains the T_d symmetry with a fairly large HOMO–LUMO energy gap (E_{HL}) of 2.62 eV, indicating high electronic stability. The vibration frequency is checked to verify that it is a true local minimum on the potential energy surface. The bond length of Al–Al is 2.59 Å, quite approaching the experimental data (2.55 Å in $Al_2H_6^{2-}$ dianion[68]). In addition, Al–C, $C{\equiv}C$, C–H bond lengths are 1.92 Å, 1.22 Å, and 1.07 Å, respectively. In order to reveal its electronic character, the AdNDP chemical bonding analysis is carried out, and the results are shown in Fig. 2b. There are one 4c–2e (four-center two-electron) σ bonds with occupancy numbers (ON) = 1.99 |e| and three 4c–2e π bonds with ON = 1.94 |e| in the Al_4 core, which could be described as super S and $P_{x,y,z}$ orbitals from orbital symmetries. Thus, the Al_4 core can be considered as a closed shell 8e SA depending on their electronic shell. More details for the AdNDP chemical bonding analysis are shown in Fig. S1 (ESI†).

Nucleus-independent chemical shift (NICS) value is capable of evaluating aromaticity, which indicates the electronic shell-closure of the delocalized bonding system.[69] Therefore, NICS-scan[70] calculation was employ to further verify the existence of the superatomic character of Al_4 core in this $Al_4(C{\equiv}CH)_4$ cluster. NICS values are scanned along the central axis of the Al_4 core and benzene within the range of −4.0 to 4.0 Å, with the positions of NICS (0) located at their geometric centers, and two curves are plotted in Fig. 2c. The minimum NICS values in Al_4 is −25.36 ppm, much smaller than that of classical aromatic benzene (−9.97 ppm).[71] This strong aromaticity indicates electron delocalization with shell-closure in the Al_4 core, which confirms the existence of the superatomic character in the Al_4 core.

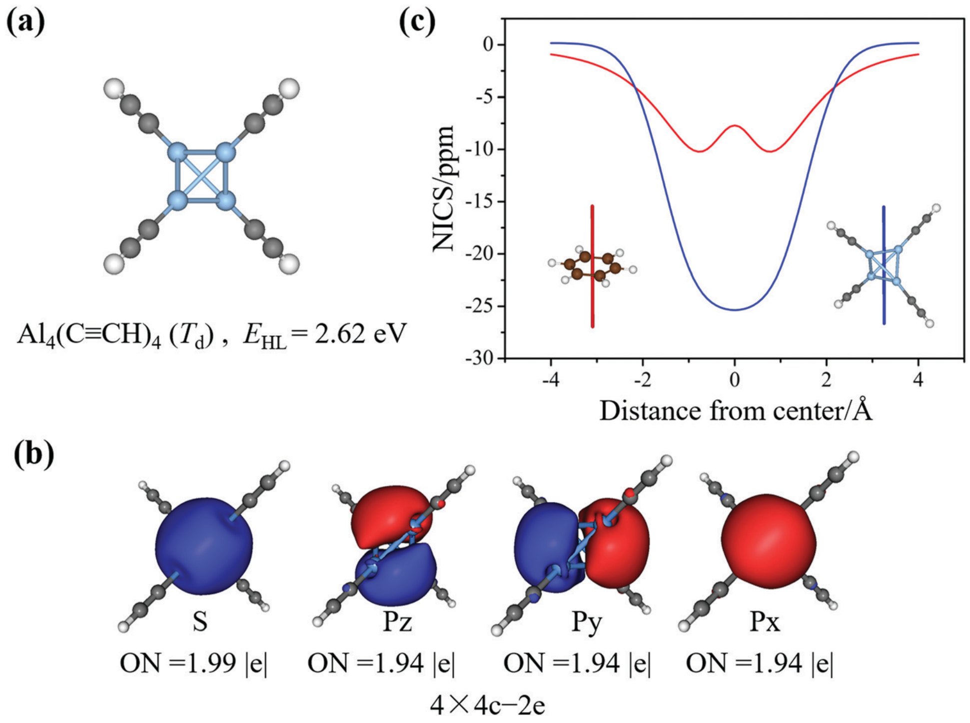

Fig. 2 (a) Optimized geometric structure of the $Al_4(C{\equiv}CH)_4$ cluster at the PBE/def2tzvp level of theory. Al, blue; C, grey; and H, white. (b) AdNDP-localized natural bonding orbitals of the $Al_4(C{\equiv}CH)_4$ cluster. (c) NICS-scan curves along the central axis of the $Al_4(C{\equiv}CH)_4$ and benzene in the range of −4.0 to 4.0 Å. The structure labelled indicates direction of the scan.

Geometric structure, stability, and properties of Al_4C_4 SOF

Followingly, Al_4C_4 crystal is assembled from the $Al_4(C{\equiv}CH)_4$ cluster based on the rules of the SAN model. Burdett and Lee[72] first noted that a carbon atom in the diamond lattice could be replaced by a carbon tetrahedron C_4 without loss of symmetry and periodicity of the crystal, and proposed a new allotropic supertetrahedral. A number of new structures have been designed through similar substitution forms, which include superterahedral boron,[73] supertetrahedral aluminum,[40] supertetrahedral gallium.[74] The Al_4C_4 unit in the $Al_4(C{\equiv}CH)_4$ cluster has the regular tetrahedron structure and a similar bonding pattern as a carbon atom in diamond, which can be extended to diamond-like bulk solid using a diamond lattice as the template. The C–C bond length in diamond is 1.54 Å, while the Al_4C_4–Al_4C_4 distance is about ~8.18 Å. Therefore, the lattice constant of the diamond unit cell is expanded from 3.57 Å to 18.96 Å. Next, each C atom is replaced by one Al_4C_4 tetrahedral unit to generate the initial Al_4C_4 crystal structure (as shown in Fig. S7, ESI†). After full geometry optimization, the Al_4C_4 system can maintain the symmetry (face-centered cubic lattice with space group 227 $FD\bar{3}M$), and the lattice constant is changed to 19.04 Å. The atomic coordinate of initial and optimized Al_4C_4 crystal (in cif format) are given in attached files.

As shown in Fig. 3a, the unit cell contains 32 Al and 32 C atoms with lattice parameters of $a = b = c = 19.04$ Å. The Al_4 cores are connected by bridged –C≡C– ligands to form superatom networks. There are three type bonds, C≡C, Al–Al, Al–C with the bond length of 1.24, 2.60, 1.92 Å, respectively, close to those in the $Al_4(C{\equiv}CH)_4$ cluster. In the Al_4 core with 12 valence electrons, 4 electrons are involved in the covalence bond with four peripheral –C≡C– ligands, and the rest 8 electrons are retained in the Al_4 core. The SSAdNDP analysis was carried out to gain a deep insight into the electronic shell in the Al_4C_4 unit. As shown in Fig. 3b, there are also S, $P_{x,y,z}$ superatom orbitals in the Al_4 core, confirming its closed-shell superatomic character. Therefore, this structure could be viewed as the SAN with the 4c–8e SA core. Moreover, there are Al–C σ bonds with ON = 1.96 |e| and C–C σ bonds with ON =1.99 |e|, as well as two C–C π bond with ON = 1.94 |e|. More details of the SSAdNDP chemical bonding analysis are shown in Fig. S2 (ESI†).

Phonon calculations are performed along the high-symmetry lines in the first Brillouin zone to confirm the dynamic stability of this Al_4C_4 crystal, and the calculated phonon dispersion is given in Fig. 3c. As carbon is a relatively light atom, C≡C vibration frequency is relatively high (appearing at 2059 cm^{-1}), which is not shown in Fig. 3c (shown in Fig. S3, ESI†). All frequencies are real and no imaginary phonon frequencies existing in the whole Brillouin zone, indicating that the structure is kinetically stable.

To discuss the thermodynamic stability of Al_4C_4, its molecular dynamics simulation is performed. A supercell is constructed, consisting of 2 × 2 × 2 primitive cells (involving 128 atoms). The simulations last for 5 ps with a time step of 1.0 fs at initial temperatures of 700 K. As shown in Fig. 4, the

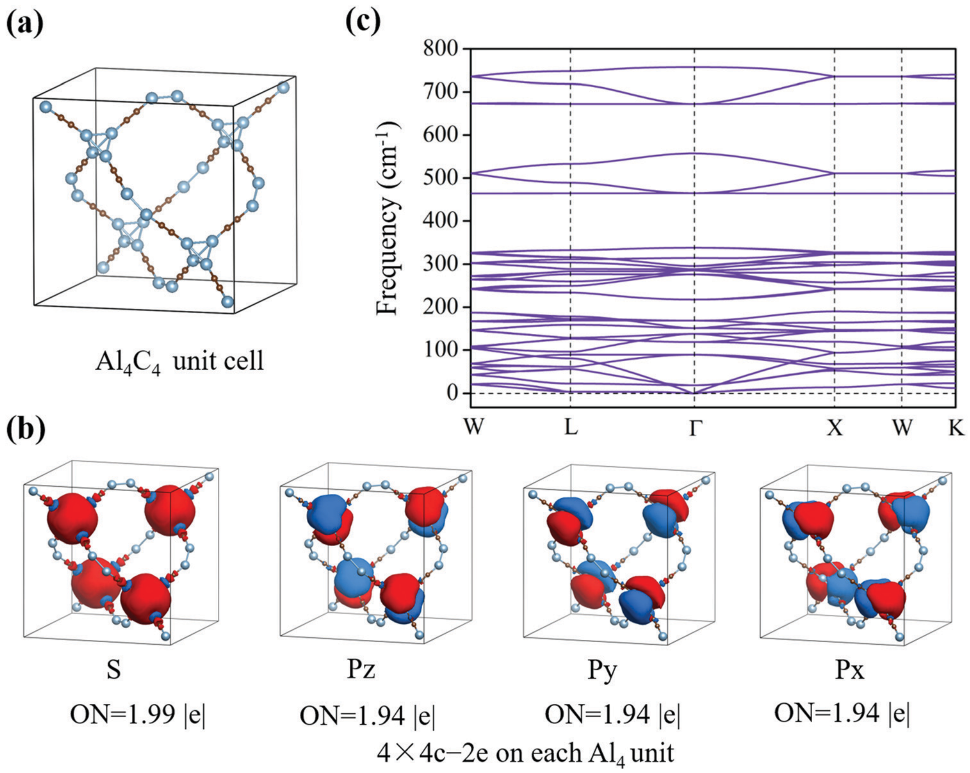

Fig. 3 (a) Optimized structure of the Al_4C_4 with unit cell. Al, blue; and C, brown. (b) SSAdNDP chemical bonding pattern of the Al_4C_4 unit. (c) Calculated phonon dispersion curves along the high-symmetry lines in the first Brillouin zone for Al_4C_4.

instantaneous energy in the system fluctuates around an average value of −705 eV, and the structure is still intact during this process, indicating its good thermal stability in a high temperature environment. In addition, snapshots of the supercell before and after the simulation are given in Fig S4 (ESI†).

Cohesive energy is further calculated to evaluate the energy stability of materials. The cohesive energy of Al_4C_4 is defined by the following equations: $E_{\mathrm{coh}} = (4E_{\mathrm{Al}} + 4E_{\mathrm{C}} - E_{\mathrm{Al4C4}})/8$, where E_{Al4C4}, E_{Al}, E_{C} are the energy of one Al_4C_4 unit containing 8 atoms, a single Al atom and a single C atom in its crystal structure, respectively. This cohesive energy is 4.71 eV per atom higher than crystalline aluminum (3.82 eV). The possible formation route is discussed through formation enthalpy calculation. Herein, Al, HC$\equiv$CH and O_2 are taken as references to evaluate the experimental feasibility of Al_4C_4. The formation enthalpy of Al_4C_4 crystal is calculated, as shown in Fig. 5. This process is an exothermic reaction with the reaction energy (ΔH) of −205.99 KJ mol^{-1}, indicating that this structure is energetically more preferable. This result gives reference for the experimental synthesis of this Al_4C_4 crystal.

The calculated elastic constants, bulk modulus, shear Modulus, Young's Modulus, Poisson's ratio, Vickers hardness and density for Al_4C_4 are given in Table 1. Poisson's ratio characterizes the elastic and plastic properties of the material. It is worth mentioning that the calculated value is 0.40 for this material, larger than the traditional structural forms of aluminum with the coefficients of 0.34, which indicates sufficiently

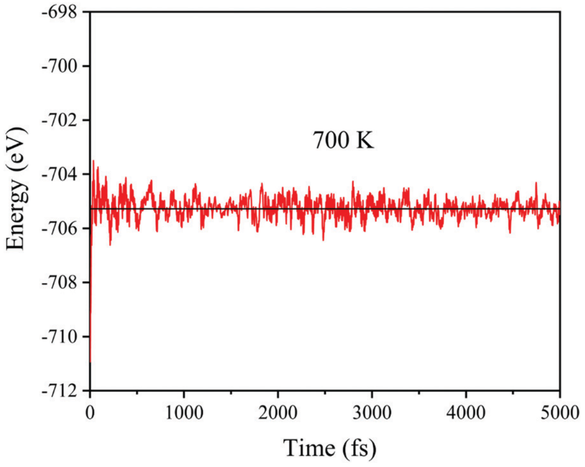

Fig. 4 Energy fluctuation depending on the simulated time step in molecular dynamics simulation at 700 K.

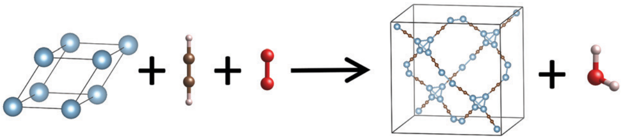

$4Al+2C_2H_2+O_2 \rightarrow Al_4C_4+2H_2O \quad \Delta H = -205.99$ KJ/mol

Fig. 5 Formation process of Al_4C_4 from Al, C_2H_2 and O_2. The reaction equation and formation enthalpy (KJ mol^{-1}) are labeled.

Table 1 Calculated elastic constants (c_{ij}, GPa), bulk modulus (K, GPa), shear modulus (G, GPa), Young's modulus (E, GPa), Poisson's ratio (ν), ρ (g cm^{-3}) and Vickers hardness (H, GPa) for the Al_4C_4 SOF crystal

Structure	c_{11}	c_{12}	c_{44}	K	G	E	ν	H_{simunek}	ρ
Al_4C_4	16.29	11.46	3.14	13.07	2.82	7.90	0.40	0.54	0.3

high plastic properties of this Al_4C_4 crystal. The small values of shear modulus, bulk modulus and elastic constant (c_{ij}) also confirm this result. The Young's modulus, which characterizes the strength characteristics of this material, is calculated to be 7.9 GPa, between lithium (4.9 GPa) and lead (18 GPa) material. The Vickers hardness (0.54 GPa) calculated by the empiric formula of Šimůnek and vackář for covalent and ionic solid states is substantially lower than that of diamond (96.0 GPa) and silicon (11.3 GPa). The density of the material is 0.30 g cm^{-3}, which can be explained by the presence of large cavities between the nearby tetrahedrane units of the structure. The diameter of the hole is approximately 13.46 Å, which shows that it is an ultra-light material.

The appearance of micropores makes it possible for the diffusion of O_2 into the structure at room temperature. The physisorption and chemisorption of an O_2 molecule on Al_4C_4 are investigated, and the pathway of the oxidation process is calculated. The strength of interactions between Al_4C_4 and O_2 is described by the binding energy, defined as: $E_{\text{bind}} = E_{\text{total}} - E_{\text{O2}} - E_{\text{Al4C4}}$, where the E_{total}, E_{O2} and E_{Al4C4} refer to the total energies of Al_4C_4–O_2, O_2 molecule, and bare Al_4C_4, respectively. Thus, the more negative the E_{bind}, the stronger the adsorption. Different adsorption sites for O_2 on Al_4C_4 and their E_{bind} of physisorption are given in Fig. S8(a)–(c) (ESI†). The geometry with the lowest E_{bind} (Fig. S8a, ESI†) is selected as the initial structure to simulate the oxidation process.

To examine the possible oxidation pathway, the transition state is investigated using the CI-NEB method. As shown in Fig. S9 (ESI†), in the initial state of physisorption (E_{bind} = −0.10 eV), the O_2 molecule is located 3.57 Å above the triangle surface of the Al_4 unit and the O–O bond length is 1.24 Å, close to the value of the dissociative O_2 molecule (1.23 Å calculated in the same theoretical level). In the transition state, the O_2 molecule is located 2.04 Å above the triangle surface of the Al_4 unit, the O–O bond length is elongated to 1.30 Å, and the Al–O bond length is 2.24 Å. The O_2 molecule undergoes a transition from physisorption to chemisorption by overcoming an activation energy (E_a) of 0.68 eV, which can be overcome at the room temperature (300 K) according to the transition-state theory (<0.7 eV).[75,76] In the final state of chemisorption, the O_2 molecule is absorbed 1.50 Å above the triangle surface of the Al_4 unit (E_{bind} = −3.64 eV), the O–O bond length is elongated to 1.56 Å and Al–O bond length is 1.91 Å. The larger adsorption energy indicates a strong interaction between Al_4C_4 and O_2. In adsorption and CI-NEB calculations, spin polarization was turned on. To determine the spin states of the initial (physisorption), transition state and final (chemisorption) structures, we also calculated the single point energies of these structures in specified singlet and triplet spin multiplicities. By comparing the energies with spin polarization and specified singlet/triplet multiplicities (Table S2, ESI†), it can be concluded that the physisorption and transition states are triplet (same as freestanding O_2 molecule), whereas it changes to the singlet state in the chemisorption structure.

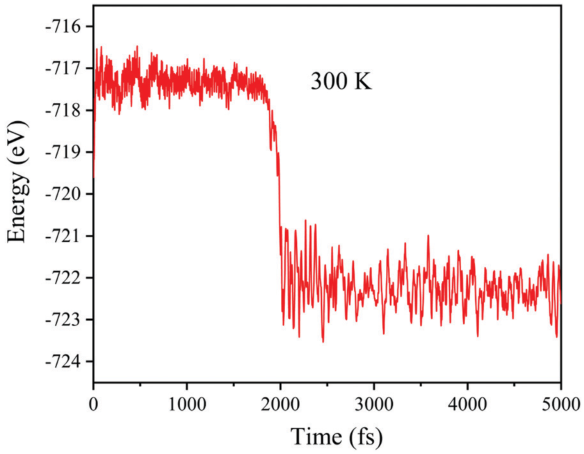

Fig. 6 Energy fluctuation depending on the simulated time step of the Al_4C_4 supercell with one O_2 molecule at 300 K.

To further confirm the results, the dynamical oxidation process is simulated at 300 K, and AIMD simulation lasts for 5 ps with a time step of 1 fs. The initial configuration is the supercell (2 × 2 × 2 primitive cell) with one O_2 molecule inside it (coordinates are given in ESI†). As shown in Fig. 6, the energy is almost unchanged before 2 ps, but drops sharply afterward. This is probably induced by the oxidation reaction of the Al_4 units, which is confirmed by the snapshots of its initial and final states (Fig. S5, ESI†).

The band structure and projected density of states (PDOS) are calculated at the PBE (Fig. S6, ESI†) and HSE06 (Fig. 7) levels of theory to further investigate the electronic properties. It can be clearly seen that the valence band maximum (VBM) is separated from the conduction band minimum (CBM), showing an indirect band gap. The band gap value is 1.87 eV at the PBE level, and is 2.57 eV at the more accurate HSE06 functional. Moreover, the analysis of PDOS reveals that the energy states near the Fermi level mainly originated from the orbitals of Al atoms.

Further exploration of optical properties for Al_4C_4 was carried on by computing their dielectric functions using the

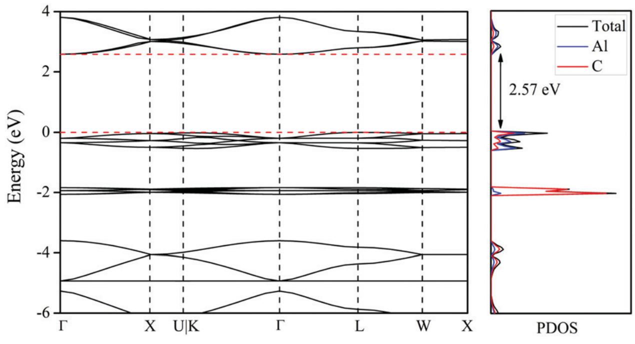

Fig. 7 Electronic band structure and PDOS of the Al_4C_4 at the HSE06 level. The Fermi level is set at zero.

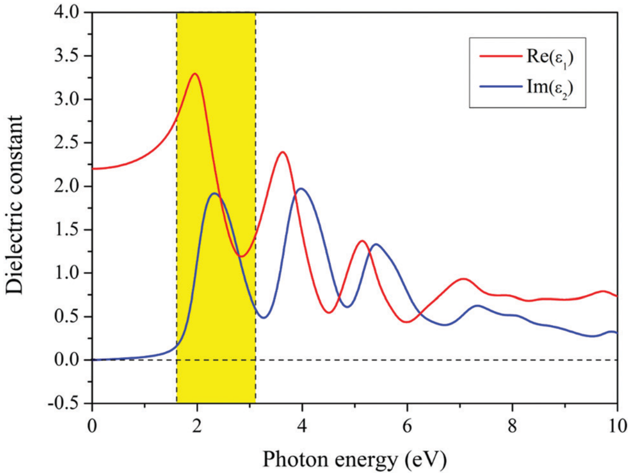

Fig. 8 Frequency dependence of the real (red curve) and imaginary (blue curve) parts of complex dielectric permittivity for the Al_4C_4 crystal.

PBE functional. The dielectric function $\varepsilon(\omega)$ is used to describe the optical properties of materials: $\varepsilon(\omega) = \varepsilon_1(\omega) + i\varepsilon_2(\omega)$, where ω is the photon frequency, $\varepsilon_1(\omega)$ is the real part and $\varepsilon_2(\omega)$ is the imaginary part of the dielectric function. Evidently, due to the crystal symmetry, the optical absorption of all structures is isotropic. The absorption peaks are observed at 532 nm (2.33 eV) in the green regions (the visible spectrum is marked in yellow). Moreover, this material has a wide optical absorption range, namely 2–6 eV, as shown in Fig. 8. They demonstrate high efficiency absorption of ultraviolet and visible lights. Therefore, the optical property analysis lists this material as quite promising candidates for optoelectronic applications.

Conclusion

In summary, a superatom organic framework (SOF) material is designed based on the SAN model. Tetrahedron Al_4 superatom unit is used as nodes in traditional MOF, and linear $-C{\equiv}C-$ ligands is chosen as linkers. First, the $Al_4(C{\equiv}CH)_4$ cluster is built and optimized with a large E_{HL} of 2.62 eV. AdNDP and NICS-scan analysis reveal that the structure follows the SAN model with a (4c–8e) closed-shell Al_4 SA core. Then, the diamond lattice is used as a template to predicted the Al_4C_4 crystal from the $Al_4(C{\equiv}CH)_4$ cluster, in which Al_4 units is connected by four $-C{\equiv}C-$ ligand to form a superatom network. SSAdNDP reveals that the Al_4 core keeps the superatomic bonding character. This structure has high dynamic and thermal stabilities depending on AIMD and formation enthalpy calculation, and it is an indirect semiconductor with a band gap of 2.57 eV at the HSE06 level. Analysis on optical properties shows that Al_4C_4 has strong absorption in the ultraviolet and visible regions, which indicates its potential application as optoelectronic material.

Our studied proposed a novel kind of SOF material. It has the high porous structure as traditional MOF and its cluster nodes keep electronic shell of SA, indicating its unique properties. This work provides a new idea for designing new functional MOF materials.

Conflicts of interest

There are no conflicts of interest to declare.

Acknowledgements

This work is financed by the National Natural Science Foundation of China (21873001, 22103001), by Natural Science Foundation of Anhui Province (2108085QB64), and by the Foundation of Distinguished Young Scientists of Anhui Province. The calculations are carried out at the High-Performance Computing Center of Anhui University.

References

1 H. C. Zhou, J. R. Long and O. M. Yaghi, *Chem. Rev.*, 2012, **112**, 673–674.
2 Y. Du, J. Gao, L. Zhou, L. Ma, Y. He, X. Zheng, Z. Huang and Y. Jiang, *Adv. Sci.*, 2019, **6**, 1801684.
3 L. Feng, J. L. Li, G. S. Day, X. L. Lv and H. C. Zhou, *Chem*, 2019, **5**, 1265–1274.
4 N. Hanikel, M. S. Prevot and O. M. Yaghi, *Nat. Nanotechnol.*, 2020, **15**, 348–355.
5 C. Li, L. Liu, J. Kang, Y. Xiao and H. Zhang, *Energy Storage Mater.*, 2020, **31**, 115–134.
6 S. W. Li, W. Wang and J. S. Zhao, *Appl. Catal., B*, 2020, **277**, 119224.
7 L. J. Small, S. E. Henkelis, D. X. Rademacher, M. E. Schindelholz, J. L. Krumhansl, D. J. Vogel and T. M. Nenoff, *Adv. Funct. Mater.*, 2020, **30**, 2006598.
8 C. Wang, F. F. Liu, Z. Tan, Y. M. Chen, W. C. Hu and X. H. Xia, *Adv. Funct. Mater.*, 2020, **30**, 1908804.
9 B. Yang, L. Ding, H. Yao, Y. Chen and J. Shi, *Adv. Mater.*, 2020, **32**, 1907152.
10 X. Zhang, R. B. Lin, J. Wang, B. Wang, B. Liang, T. Yildirim, J. Zhang, W. Zhou and B. Chen, *Adv. Mater.*, 2020, **32**, 1907995.
11 H. Furukawa, K. E. Cordova, M. O'Keeffe and O. M. Yaghi, *Science*, 2013, **341**, 1230444.
12 O. M. Yaghi, G. Li and H. Li, *Nature*, 1995, **378**, 703–706.
13 H. Li, K. Wang, Y. Sun, C. T. Lollar, J. Li and H.-C. Zhou, *Mater. Today*, 2018, **21**, 108–121.
14 J.-R. Li, J. Sculley and H.-C. Zhou, *Chem. Rev.*, 2012, **112**, 869–932.
15 M. C. Wasson, C. T. Buru, Z. Chen, T. Islamoglu and O. K. Farha, *Appl. Catal., A*, 2019, **586**, 117214.
16 I. Abánades Lázaro and R. S. Forgan, *Coord. Chem. Rev.*, 2019, **380**, 230–259.
17 Y. Zhang, S. Yuan, G. Day, X. Wang, X. Yang and H.-C. Zhou, *Coord. Chem. Rev.*, 2018, **354**, 28–45.
18 X. Zhang, Z. Chen, X. Liu, S. L. Hanna and O. K. Farha, *Chem. Soc. Rev.*, 2020, **49**, 7406–7427.
19 W. Lu, Z. Wei, Z. Y. Gu, T. F. Liu, J. Park, J. Park, J. Tian, M. Zhang, Q. Zhang and T. Gentle Iii, *Chem. Soc. Rev.*, 2014, **43**, 5561–5593.

20 S. Yuan, L. Feng, K. Wang, J. Pang, M. Bosch, C. Lollar, Y. Sun, J. Qin, X. Yang, P. Zhang, Q. Wang, L. Zou, Y. Zhang, L. Zhang, Y. Fang, J. Li and H. C. Zhou, *Adv. Mater.*, 2018, **30**, 1704303.
21 L. Feng, K. Y. Wang, G. S. Day and H. C. Zhou, *Chem. Soc. Rev.*, 2019, **48**, 4823–4853.
22 S. N. Khanna and P. Jena, *Phys. Rev. Lett.*, 1992, **69**, 1664–1667.
23 S. N. Khanna and P. Jena, *Phys. Rev. B: Condens. Matter Mater. Phys.*, 1995, **51**, 13705–13716.
24 D. E. Bergeron, P. J. Roach, A. W. Castleman, Jr., N. O. Jones and S. N. Khanna, *Science*, 2005, **307**, 231–235.
25 A. C. Reber, S. N. Khanna and A. W. Castleman, *J. Am. Chem. Soc.*, 2007, **129**, 10189–10194.
26 L. Cheng and J. Yang, *J. Chem. Phys.*, 2013, **138**, 141101.
27 L. Cheng, Y. Yuan, X. Zhang and J. Yang, *Angew. Chem., Int. Ed.*, 2013, **52**, 9035–9039.
28 P. Jena and Q. Sun, *Chem. Rev.*, 2018, **118**, 5755–5870.
29 Q. Zheng, C. Xu, X. Wu and L. Cheng, *ACS Omega*, 2018, **3**, 14423–14430.
30 S. Jin, X. Zou, L. Xiong, W. Du, S. Wang, Y. Pei and M. Zhu, *Angew. Chem., Int. Ed.*, 2018, **57**, 16768–16772.
31 Q. Liu, C. Xu, X. Wu and L. Cheng, *Nanoscale*, 2019, **11**, 13227–13232.
32 K. E. Schriver, J. L. Persson, E. C. Honea and R. L. Whetten, *Phys. Rev. Lett.*, 1990, **64**, 2539–2542.
33 W. A. De Heer, *Rev. Mod. Phys.*, 1993, **65**, 611–676.
34 D. E. Bergeron, A. W. Castleman, Jr., T. Morisato and S. N. Khanna, *Science*, 2004, **304**, 84–87.
35 A. W. Castleman and S. N. Khanna, *J. Phys. Chem. C*, 2009, **113**, 2664–2675.
36 S. N. Khanna and P. Jena, *Phys. Rev. Lett.*, 1992, **69**, 1664–1667.
37 S. A. Claridge, A. W. Castleman, Jr., S. N. Khanna, C. B. Murray, A. Sen and P. S. Weiss, *ACS Nano*, 2009, **3**, 244–255.
38 Q. Liu, C. Zhang, C. Xu, S. Hu and L. Cheng, *Phys. Chem. Chem. Phys.*, 2020, **22**, 3921–3926.
39 R. M. Minyaev, I. V. Getmanskii and V. I. Minkin, *Russ. J. Inorg. Chem.*, 2014, **59**, 332–336.
40 I. V. Getmanskii, V. V. Koval, R. M. Minyaev, A. I. Boldyrev and V. I. Minkin, *J. Phys. Chem. C*, 2017, **121**, 22187–22190.
41 I. V. Getmanskii, V. V. Koval, A. I. Boldyrev, R. M. Minyaev and V. I. Minkin, *J. Phys. Chem. A*, 2019, **123**, 267–271.
42 M. J. Frisch, *et al.*, *Gaussian 09, Revision B.01*, Gaussian, Inc., Wallingford, CT, 2009.
43 C. Adamo and V. Barone, *J. Chem. Phys.*, 1999, **110**, 6158–6170.
44 F. Weigend and R. Ahlrichs, *Phys. Chem. Chem. Phys.*, 2005, **7**, 3297–3305.
45 G. Kresse and J. Hafner, *Phys. Rev. B: Condens. Matter Mater. Phys.*, 1993, **47**, 558–561.
46 G. Kresse and J. Hafner, *Phys. Rev. B: Condens. Matter Mater. Phys.*, 1994, **49**, 14251–14269.
47 G. Kresse and J. Furthmüller, *Comput. Mater. Sci.*, 1996, **6**, 15–50.
48 G. Kresse and J. Furthmüller, *Phys. Rev. B: Condens. Matter Mater. Phys.*, 1996, **54**, 11169–11186.
49 P. E. Blöchl, *Phys. Rev. B: Condens. Matter Mater. Phys.*, 1994, **50**, 17953–17979.
50 G. Kresse and D. Joubert, *Phys. Rev. B: Condens. Matter Mater. Phys.*, 1999, **59**, 1758–1775.
51 J. P. Perdew, K. Burke and M. Ernzerhof, *Phys. Rev. Lett.*, 1996, **77**, 3865–3868.
52 J. Heyd, G. E. Scuseria and M. Ernzerhof, *J. Chem. Phys.*, 2003, **118**, 8207–8215.
53 H. J. Monkhorst and J. D. Pack, *Phys. Rev. B: Condens. Matter Mater. Phys.*, 1976, **13**, 5188–5192.
54 A. Togo and I. Tanaka, *Scr. Mater.*, 2015, **108**, 1–5.
55 G. Henkelman, B. P. Uberuaga and H. Jónsson, *J. Chem. Phys.*, 2000, **113**, 9901–9904.
56 L. A. Burns, Á. V. Mayagoitia, B. G. Sumpter and C. D. Sherrill, *J. Chem. Phys.*, 2011, **134**, 084107.
57 M. L. K. a. M. T. G. J. Martyna, *J. Chem. Phys.*, 1992, **97**, 2635–2643.
58 D. Y. Zubarev and A. I. Boldyrev, *Phys. Chem. Chem. Phys.*, 2008, **10**, 5207–5217.
59 T. R. Galeev, B. D. Dunnington, J. R. Schmidt and A. I. Boldyrev, *Phys. Chem. Chem. Phys.*, 2013, **15**, 5022–5029.
60 G. Liu, N. Fedik, C. Martinez-Martinez, S. M. Ciborowski, X. Zhang, A. I. Boldyrev and K. H. Bowen, *Angew. Chem., Int. Ed.*, 2019, **58**, 13789–13793.
61 N. Fedik, M. Kulichenko, D. Steglenko and A. I. Boldyrev, *Chem. Commun.*, 2020, **56**, 2711–2714.
62 J. Czekner, L. F. Cheung, G. S. Kocheril, M. Kulichenko, A. I. Boldyrev and L.-S. Wang, *Angew. Chem., Int. Ed.*, 2019, **58**, 8877–8881.
63 N. Fedik, A. I. Boldyrev and A. Muñoz-Castro, *Phys. Chem. Chem. Phys.*, 2019, **21**, 25215–25219.
64 N. V. Tkachenko, D. Steglenko, N. Fedik, N. M. Boldyreva, R. M. Minyaev, V. I. Minkin and A. I. Boldyrev, *Phys. Chem. Chem. Phys.*, 2019, **21**, 19764–19771.
65 D. Steglenko, R. M. Minyaev, V. I. Minkin and A. I. Boldyrev, *J. Phys. Chem. Lett.*, 2018, **9**, 6963–6966.
66 B. D. Dunnington and J. R. Schmidt, *J. Chem. Theory Comput.*, 2012, **8**, 1902–1911.
67 K. Momma and F. Izumi, *J. Appl. Crystallogr.*, 2011, **44**, 1272–1276.
68 S. J. Bonyhady, N. Holzmann, G. Frenking, A. Stasch and C. Jones, *Angew. Chem., Int. Ed.*, 2017, **56**, 8527–8531.
69 P. v. R. Schleyer, C. Maerker, A. Dransfeld, H. Jiao and N. J. R. van Eikema Hommes, *J. Am. Chem. Soc.*, 1996, **118**, 6317–6318.
70 A. Stanger, *J. Org. Chem.*, 2006, **71**, 883–893.
71 P. v. R. Schleyer, M. Manoharan, Z.-X. Wang, B. Kiran, H. Jiao, R. Puchta and N. J. R. van Eikema Hommes, *Org. Lett.*, 2001, **3**, 2465–2468.
72 J. K. Burdett and S. Lee, *J. Am. Chem. Soc.*, 1985, **107**, 3063–3082.
73 I. V. Getmanskii, R. M. Minyaev, D. V. Steglenko, V. V. Koval, S. A. Zaitsev and V. I. Minkin, *Angew. Chem., Int. Ed.*, 2017, **56**, 10118–10122.
74 I. V. Getmanskii, V. V. Koval, A. I. Boldyrev, R. M. Minyaev and V. I. Minkin, *J. Comput. Chem.*, 2019, **40**, 1861–1865.
75 K. J. Laidler and M. C. King, *J. Phys. Chem.*, 1983, **87**, 2657–2664.
76 J. Wang, L. Ma, Q. Yuan, L. Zhu and F. Ding, *Angew. Chem., Int. Ed.*, 2011, **50**, 8041–8045.